Optik - International Journal for Light and Electron Optics 286 (2023) 170983

Contents lists available at ScienceDirect

Optik

journal homepage: www.elsevier.com/locate/ijleo

Non-linear optical behavior of gold and silver clusters adsorbed on 2,9-Dimethylquinacridone

Shradha Lakhera [a], Meenakshi Rana [a,*], Kamal Devlal [a], Vivek Dhuliya [b], Nupur Pandey [c]

[a] Department of Physics, School of Sciences, Uttarakhand Open University, Haldwani 263139, Uttarakhand, India
[b] Department of Physics, Gurukula Kangri (Deemed to be University), Haridwar 249404, Uttarakhand, India
[c] Photophysics Laboratory, Department of Physics, Centre of Advanced Study, DSB Campus, Kumaun University, Nainital 263002, Uttarakhand, India

ARTICLE INFO

Keywords:
Clusters
Density functional theory
Nonlinear optics
2,9-Dimethylquinacridone
Hyperpolarizability

ABSTRACT

In the present work, the adsorption of silver (Ag_3) and gold (Au_3) clusters on 2,9-Dimethylquinacridone (2,9-DMQA) was examined by using density functional theory. The variation of structural parameters was observed after the introduction of Ag_3 and Au_3 clusters. The interactions between the clusters and 2,9-DMQA induced variations in the structural parameters and electronic properties. The involvement of clusters in inducing the intramolecular charge transfer was confirmed by electrostatic potential surface and charge analysis. The electronic properties of the complex were studied by absorption and emission spectra. The adsorption of the Ag_3 and Au_3 clusters over the 2,9-DMQA leads to an enormous rise in the hyperpolarizability of the complexes. Thus, the Ag_3 and Au_3 clusters adsorbed 2,9-DMQA gave enhanced nonlinear optical activity.

1. Introduction

Over the past three decades, great scientific efforts have been made to design new organically derived nonlinear optical (NLO) materials with ultrafast response time and higher efficiency [1]. The development of organic NLO materials has become one of the most crucial areas of research among researchers due to their potential applications. Organic compounds with superior NLO properties have been extensively studied owing to their broad applications in the areas of microscopy, telecommunications, microfabrication, three-dimensional data storage, frequency mixing, optical power limiting, up-converted lasing, photodynamic therapy, lasers, and photoluminescence [2–5]. Researchers are in the queue to explore different NLO materials comprising molecular dyes, polymers, nanomaterials, and organic, and inorganic semiconductors. The π-extended skeletal compounds have developed a new and trending sphere in the field of NLO materials due to high durability, high structural flexibility, exceptional photo-thermal stability, unique electronic optic spectra, and short response time [6,7]. Organic π-conjugated compounds are rich in electron donors and electron acceptors that lead to intramolecular charge transfer (ICT) [8–10]. Ultimately, rising ICT leads to a rise in hyperpolarizability and NLO responses of the molecules [11]. Thus, the NLO activity of any compound can be enhanced by simply introducing some donor-acceptor moieties [12]. Literature has evidenced a lot of studies reporting the enhancement of ICT by optimizing the externally added donor/acceptor pairs that could finally maximize the NLO responses. The aforementioned features were used for the enhancement of

* Corresponding author.
E-mail address: mrana@uou.ac.in (M. Rana).

https://doi.org/10.1016/j.ijleo.2023.170983
Received 21 December 2022; Received in revised form 25 April 2023; Accepted 18 May 2023
Available online 19 May 2023

NLO responses of many compounds like 6,12-Diethynylindeno[1,2-*b*] fluorenes [13], phenoxazine [14], triphenylamine derivative [15], chromophores with double carboxyl groups [16], optical chromophores with different aromatic amine donors [17], phenanthrolines [18], Cyclometallated iridium (III) complexes [19], and many more. Structural arrangements of (2-cyano-5-(4-(phenyl (4-vinylphenyl)amino)phenyl) penta-2,4-dienoic acid (TC4) was altered by Asif et al. and its NLO activity using DFT tools [20]. Some dyes like indigo-based dyes with high non-linear optical response have been investigated by Mahmood et al. [21]. DFT was used to study the electronic, NLO, and vibrational properties of indigo and newly designed dyes (IM-Dye-0, IM-Dye-1, IM-Dye-2, and IM-Dye-3). A detailed computational analysis is performed on the chalcogen-based polymers by Mahmood for employing the polymers as efficient NLO materials and charge transport materials [22]. Thus, DFT analysis has been considered as a game changer, especially in the fabrication of NLO and photovoltaics.

Heterocyclic aromatic hydrocarbons such as anthracenes, pyrenes, indole, quinoline, pyrene, coronene, chrysene, naphthalene, fluorene, benzopyrene, etc., are the compounds containing multiple benzene rings clubbed together in different arrangements like linear, angular and clusters [23–25]. These molecules are known for their excellent performance and high charge carrier mobility [26]. Thus, researchers have a profound interest in developing various applications for these molecules. Quinacridone (QA) is one such polycyclic aromatic hydrocarbon that is organically prepared by condensation followed by dehydrogenation of succinosuccinate esters with aniline [27]. QA is a pink-colored powder that is used in high-quality dyes and paints [28]. In a dispersed state, QA shows an intense fluorescence [29]. Due to having high carrier mobility and fluorescence, it can be favorably used in optoelectronic devices, organic field effect transistors, organic light-emitting diodes, organic solar cells, photovoltaics, and many others [30]. The self-assembling property of QA due to intermolecular hydrogen bonding and π-conjugated bonds makes it a desirable supramolecular organic semiconductor [31]. The investigation of third-order NLO properties of different quinacridone derivatives like dimethyl vinyl quinacridone, methoxy quinacridone, and N, N-dimethylamine quinacridone [32], 5,12-dioctylquinolino[2,3-*b*]acridine-7,14-dione [33], 5,12-Biphenyl-5,12-dihydroquinolino[2,3-*b*]acridine-7,14-dione, and 5,12-Bis(4-methoxyphenyl)-5,12-dihydroquinolino[2, 3-*b*]acridine-7,14-dione have been performed by Jia et al. [34]. Felscia has reported a rise in the NLO activity of probe QA after the adsorption of gold and silver clusters [35]. The identification of luminescence of QA hierarchical microstructures was done by Deska et al. [36]. Apart from these, the QA and its derivatives were employed for many other applications like solar cells [37], photovoltaics [38], light-emitting diodes [39], lasers [40], dyes [41], and many more.

The present study accounts for the investigation of NLO responses of QA derivative 2,9-Dimethylquinacridone (2,9-DMQA) with adsorbed silver (Ag_3) and gold (Au_3) metal clusters in different solvents. The planar structure of 2,9-DMQA forms strong intermolecular π-π interactions leading to high NLO activity. The availability of nitrogen atoms makes 2,9-DMQA donating, and the introduction of an electron-withdrawing unit can readily give rise to the ICT character of 2,9-DMQA. Thus, to increase the NLO characteristics of 2,9-DMQA, silver (Ag_3) and gold (Au_3) metal clusters have been introduced near the chemically reactive areas and the adsorption of clusters on 2,9-DMQA was observed. Ag_3 and Au_3 trimers are firstly obtained after the nucleation of silver and gold nanoparticles and many research reporting adsorption studies of metal trimers have resulted in an enormous rise in the NLO activity [42]. The computational study comprises establishing the enhancement of ICT in 2,9-DMQA after the introduction of Ag_3 and Au_3 using density functional theory (DFT). The chemical reactivity was analyzed by natural bond orbital analysis (NBO) and chemical reactivity parameters. The simulated vibrational, absorption, and emission spectra give complete spectral features.

2. Computational methods

The simulation tools like DFT are getting immense interest from researchers due to their skillful properties and versatility in quantum computations [43–46]. One gets a varied set of functions to get the calculations done and even the results can be relayed [47]. Even the literature has evidenced that the simulation results specially generated by DFT were found to be satisfying corresponding to the experimental results [48–50]. The PDB structure of 2,9-DMQA is available on the online database PubChem (https://pubchem.ncbi.nlm.nih.gov/) with ID 70423. Two different kinds of hybrid functionals were used for the calculations with the Gaussian 09 program's package (https://gaussian.com/). The analysis of chemical and spectral properties was analyzed using Gauss View (https://gaussian.com/gaussview6/). All the quantum chemical calculations for probe 2,9-DMQA were done using the B3LYP/6-311-G(++d,p) set of functions [51]. The set of functions was known to be more accurate and precise for calculations of organic compounds. Ag_3 and Au_3 trimers were drawn nearby the identified chemically reactive sites of the optimized structures of 2,9-DMQA using the builder function of the Gauss View 5.0 program. 2,9-DMQA + Ag_3 and 2,9-DMQA + Au_3 were optimized employing the DFT augmented with B3PW91 (Becke exchange & Perdew and Wang in 1991 correlation functional) with LanL2DZ basis set The B3PW91/LanL2DZ functions are widely used to predict the interactions between the organic compounds and the metal clusters [52]. The structure was minimized for the values maximum force as 0.00045, Root-mean-square (RMS) force 0.0003, maximum displacement 0.0018, and RMS displacement 0.0012 without any additional information sets. The free energy was also calculated and computed for the 2, 9-DMQA and clusters molecule by the following given expression:

$$E_{free} = E_{electronic} + E_{thermal} \tag{1}$$

Interaction energy for the 2,9-DMQA + Ag_3 and 2,9-DMQA + Au_3 was computed using the expression:

$$E_{\text{int}} = E_{complex} - \left(\Sigma E_{component}\right) \tag{2}$$

The better insights into the interactions between the 2,9-DMQA and clusters, basis set superposition error (BSSE) was computed for the PD-Ag_3 and PD-Au_3 with the same set of functions as used for the optimization with counterpoise = 2 procedure [53]. The

empirical dispersion term was computed for the 2,9-DMQA + Ag_3 and 2,9-DMQA + Au_3 using the "Dispersion energy = Grimme GD3" procedure for the B3PW91/LANL2DZ set of functions [54]. The optimization energies, geometrical parameters, dipole moment, and charge distribution have been estimated to predict the chemical stability of the 2,9-DMQA. The natural bond orbital (NBO) calculations were performed to report the ICT within the molecule and the clusters. The second-order perturbation approach was used for computing the stabilization energy (*E(2)*) corresponding to each donor (i) and acceptor (j) atom [55]. The *E(2)* corresponding to the delocalization of each $i \rightarrow j$ was calculated using the expression:

$$E(2) = \Delta E_{ij} - q_i \left(\frac{f_{ij}^2}{E_j - E_i} \right) \tag{3}$$

where *F(i,j)* is the Fock matrix element between i and j NBO orbitals, ΔE_{ij} is the energy corresponding to each NBO interaction, E_j and E_i are the energies of the acceptor and donor NBOs. Furthermore, evidence of intramolecular interactions was established by the interpretation of molecular electrostatic potential (MEP) map and frontier molecular orbitals (FMOs). The energies corresponding to the highest occupied and lowest unoccupied molecular orbitals (HOMO-LUMO energies) are taken into account to calculate the reactivity parameters following Koopman's theorem [55-57]. The expressions for calculating different FMO parameters are as follows:

$$\Delta E = E_{LUMO} - E_{HOMO} \tag{4}$$

$$IP = -E_{HOMO} \tag{5}$$

$$EA = -E_{LUMO} \tag{6}$$

$$CP = \frac{E_{HOMO} + E_{LUMO}}{2} \tag{7}$$

$$\chi = \frac{(IP + EA)}{2} \tag{8}$$

$$\eta = \frac{E_{LUMO} - E_{HOMO}}{2} \tag{9}$$

$$S = \frac{1}{\eta} \tag{10}$$

$$\omega = \frac{\mu^2}{2\eta} \tag{11}$$

$$\omega^+ = \frac{(IP + 3EA)^2}{16(IP - EA)} \tag{12}$$

$$\omega^- = \frac{(3IP + EA)^2}{16(IP - EA)} \tag{13}$$

Time-dependent Self-consistency field theory (TD-SCF) was used for computing the absorption and emission properties. Convergence parameters were set on the RMS density matrix at 1.00×10^{-8} and the maximum density matrix at 1.00×10^{-6} for TD-SCF calculations without any additional set of information. The absorption spectra was obtained by doing energy optimization of the optimized structure using TD-SCF function for nine transitions. The ground state optimization was further done with the resultant geometry obtained by the energy optimization for nine states for obtaining the emission spectra.

The adsorption of the clusters on the surface of the title molecule was studied using vibrational modes. The vibrational spectra were computed for 2,9-DMQA, 2,9-DMQA + Ag_3, and 2,9-DMQA + Au_3 and vibrational modes were analyzed for high Raman intensity. The Raman intensity was computed using the given expression:

$$I = \frac{f(\nu_o - \nu_i)^4 \quad S_i}{\nu_i \left[1 - \exp\left(-\frac{hc\nu_i}{K_B T} \right) \right]} \tag{14}$$

where *I* refer to Raman intensity of the considered mode, *f* is a constant with value 10^{-12}, ν_o has value 9398.5 cm^{-1}. ν_i and S_i is the vibrational wavenumber and Raman activity of selected mode respectively. h is Planck constant with value 4.1357×10^{-15} eV K^{-1}, c is speed of light having value 3×10^8 m/s, K_B is Boltzmann constant with value 8.6173×10^{-5} eV K^{-1}, and T is temperature 293.5 K.

The linear and non-linear optical activity of the molecule and the complex were predicted using polarizability and hyperpolarizability parameters respectively. These parameters were the coefficients of Taylor's series expansion of the energy of the molecules in the electric field. The linear and non-linear optical activity of the 2,9-DMQA, 2,9-DMQA + Ag_3, 2,9-DMQA + Au_3 was computed using finite field theory and were computed using the below-given expressions:

$$\alpha_{total} = \frac{1}{2}\left(\alpha_{xx} + \alpha_{yy} + \alpha_{zz}\right) \tag{15}$$

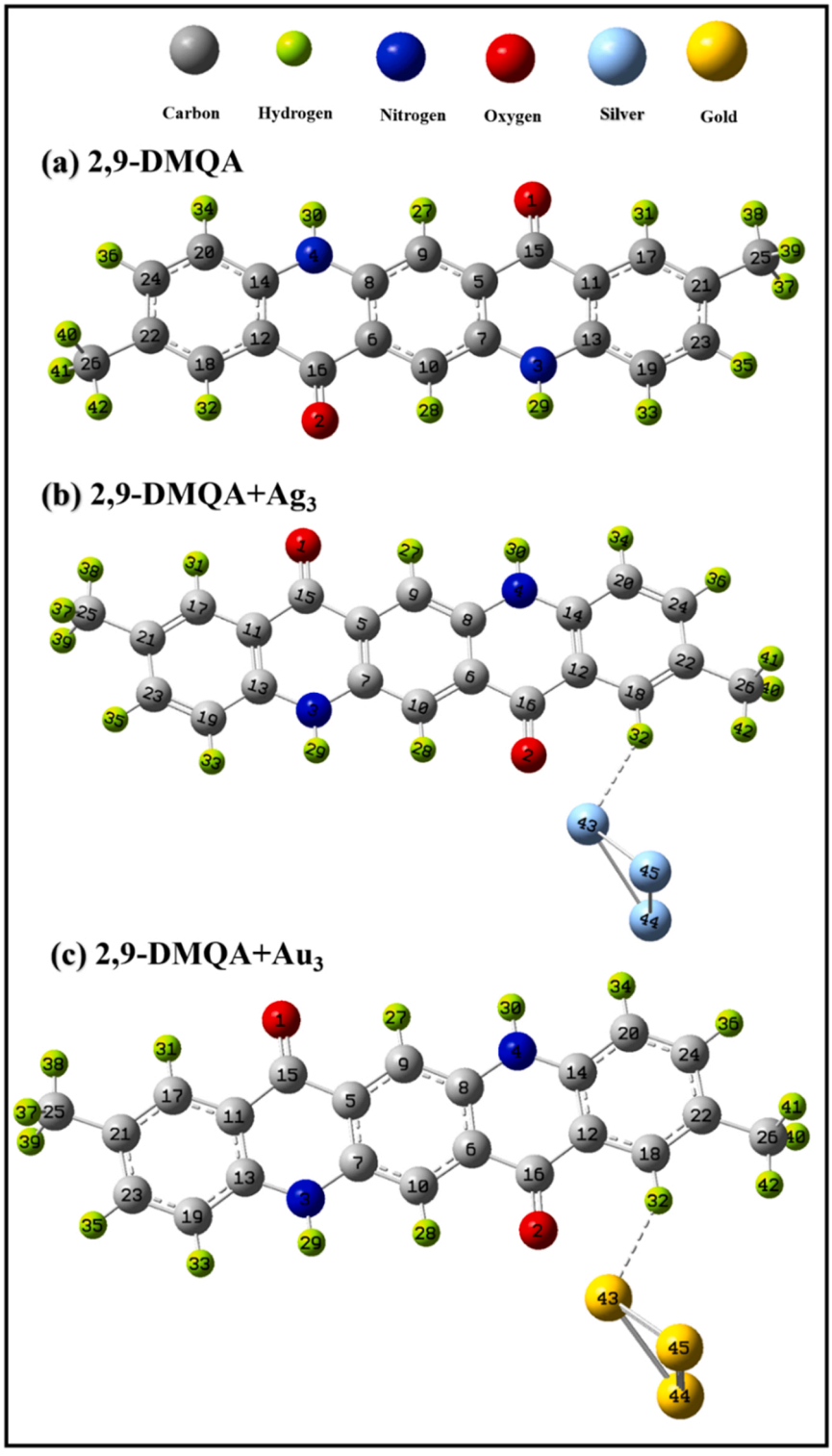

Fig. 1. Optimized geometry of (a) probe 2,9-DMQA and 2,9-DMQA adsorbed with (b) Ag_3 and (c)Au_3 computed by B3PW91/LANL2DZ.

$$\Delta\alpha = \frac{1}{\sqrt{2}}\left[\left(\alpha_{xx}-\alpha_{yy}\right)^2+\left(\alpha_{yy}-\alpha_{zz}\right)^2+\left(\alpha_{zz}-\alpha_{xx}\right)^2+6\alpha_{xz}^2+6\alpha_{xy}^2+6\alpha_{yz}^2\right]^{\frac{1}{2}} \quad (16)$$

$$\beta_{total} = \left[\left(\beta_{xxx}+\beta_{xyy}+\beta_{xzz}\right)^2+\left(\beta_{yyy}+\beta_{yzz}+\beta_{yxx}\right)^2+\left(\beta_{zzz}+\beta_{zxx}+\beta_{zyy}\right)^2\right]^{\frac{1}{2}} \quad (17)$$

where α_{xx}, α_{yy}, and, α_{zz} are the tensor components of polarizability, and β_{xxx}, β_{yyy}, and β_{zzz} *are* the tensor components of hyperpolarizability.

3. Results and discussion

3.1. Structural analysis

The ground state geometries of 2,9-DMQA in probe state and after the adsorption of Ag and Au dimers, trimers, and tetramers as performed and the optimized geometries of trimers are shown in Fig. 1. The optimized structures of dimer and trimer complex are shown in SD 1. All the optimal bond lengths and bond angles has been listed in SD 2, and 3. The benzene chains of 2,9-DMQA are planarly arranged with 40H—26C—41H and 37H—25C—39H bond angles leading to non-planarity in the molecule. The probe molecule has a low dipole moment of 7×10^{-4} Debye. This may be due to the symmetrical structure of 2,9-DMQA. A significant change in the bond length of the C═O and N—H bonds was observed which shows the mentioned bonds induce the reactivity of the 2,9-DMQA. Bonds 2O═16C and 1O═15C have a bond length of 1.26 Å and 4N—30H and 3N—29H have a bond length of 1.01 Å. A high magnitude of the bond length between the Ag and Au atoms was observed when the metal clusters were introduced into the system. Dipole moment was also computed for 2,9-DMQA, 2,9-DMQA + Ag_3, and 2,9-DMQA + Au_3 (Table 1). The justification of the selection of Ag and Au trimers was validated by computing the dipole moment for 2,9-DMQA + Ag_2, 2,9-DMQA + Ag_4, 2,9-DMQA + Au_2, and 2,9-DMQA + Au_4 (Table 1). The computed values had been listed in Table 1. The dipole moment of the 2,9-DMQA + Ag_3 does not seem to rise much (0.54 Debye). Moreover, the dipole moment of 2,9-DMQA + Au_3 (6.95 Debye) was the highest among all the other considered complexes. This might be due to the high electronegativity of Au as compared to the Ag element and the higher stability of Au trimer than the corresponding dimer and tetramer. The computed energies of the geometries were listed in Table 1. By the means of the ground state energy, we tried to justify the stability of the molecules as the lower energy means higher stability [58]. The stability (via total energy) as compared for the dimer, trimer, and tetramer adsorbed molecules for two different types of dopants i.e., Ag and Au. In simple words, total energy of 2,9-DMQA + Ag_2 was compared with 2,9-DMQA + Au_2, 2,9-DMQA + Ag_3 was compared with 2,9-DMQA + Au_3, and 2,9-DMQA + Ag_4 was compared with 2,9-DMQA + Au_4, and in all the cases the energy for Au complexes was found lower as compared to their respective Ag complexes. Moreover, in the similar context, the free energy was also found to be highest for 2,9-DMQA + Au_3 showing its highest thermodynamic stability and effectivity towards doing work in thermodynamic environment. Therefore, it can be said that the involvement of Ag_3 and Au_3 clusters in 2,9-DMQA leads to enhancement in the intramolecular interactions. Moreover, the trimers are found to give more promising results than the dimers and tetramers of the clusters. Less negative interaction energy was obtained for the 2,9-DMQA + Au_3. This validates the greater extent of interaction between 2,9-DMQA and Au_3 cluster. Moreover, the free energy and the dispersion energy were higher for 2,9-DMQA + Au_3. This is in good agreement with the dipole moment. Therefore, the larger dipole moment leads to higher intramolecular interactions in 2,9-DMQA + Au_3.

3.2. Molecular electrostatic potential surface analysis

MEP surface is applicative in qualitatively locating the electrophilic and nucleophilic sites of the molecules. It is used to illustrate the charge distribution of the molecules three-dimensionally. The distinct color blue symbolizes the molecular part having excess electrons for charge transfer and thus indicate the most electron-donating part, and the red color represents the moiety with electron-deficient part and thus indicates the electron-withdrawing part of the molecules [59]. To signify the electron-donating and electron-withdrawing moieties, the MEP surface has been mapped over the geometries of molecular systems 2,9DMQA, 2,9DMQA + Ag_3, and 2,9-DMQA + Au_3 (Fig. 2). For the probe molecule, the blue color was observed over N—H bonds and the red colored surface was observed over the C═O bonds. The settlement of red colored surface over 2O═16C and 1C═15O bonds attached

Table 1
Dipole moment (μ), Ground state energies (E_{gs}), Free energy (E_{free}), Interaction energy (E_{int}), Basis set superposition error (*BSSE*), and Dispersion energy ($E_{dispersion}$) of the 2,9-DMQA, 2,9-DMQA + Ag_3, and 2,9-DMQA + Au_3. The dipole moment is in Debye and all energies are in kcal/mol.

Complex	μ	E_{gs}	E_{free}	E_{int}	*BSSE*	$E_{dispersion}$
2,9-DMQA	7×10^{-4}	-694,924.78	-694,703.00	-	-	-
2,9-DMQA + Ag_2	5.77	-865,025.23	-542,670,095.67	-204.44	0.00468	-32.768
2,9-DMQA + Ag_3	0.54	-969,465.37	-608,206,467.45	-302.71	0.00368	-33.286
2,9-DMQA + Ag_4	3.65	-1,060,994.09	-665,640,267.01	-339.13	0.00398	-39.263
2,9-DMQA + Au_2	5.77	-865,025.23	-542,670,095.67	-195.68	0.00457	-32.97
2,9-DMQA + Au_3	6.95	-3,975,070.27	-2,493,798,069.31	-23.31	0.00435	-35.614
2,9-DMQA + Au_4	6.49	-1,035,130.06	-649,410,270.66	-21.24	0.00467	-41.34

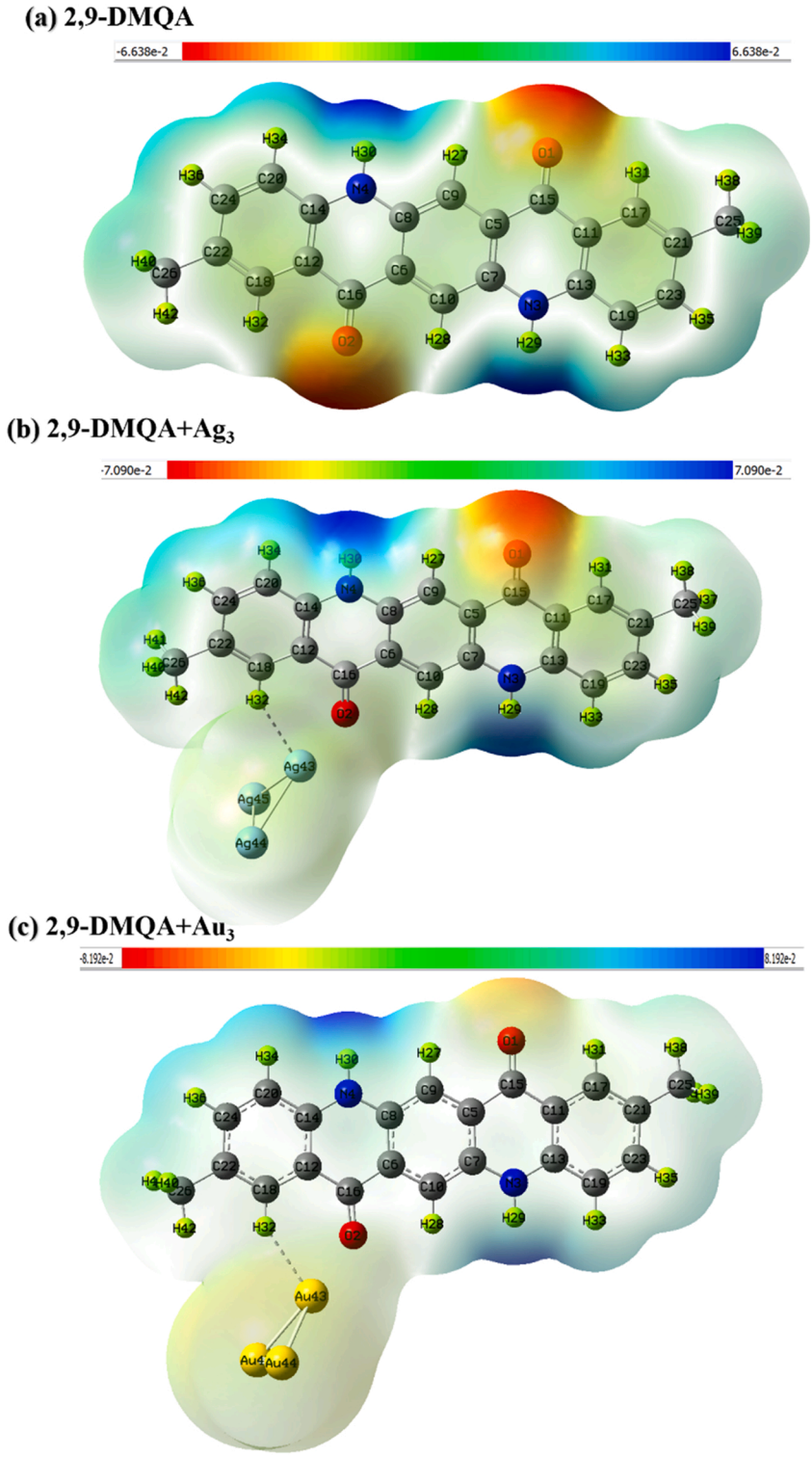

Fig. 2. MEP surface of (a) 2,9-DMQA, (b) 2,9-DMQA + Ag_3 and (c) 2,9-DMQA + Au_3 computed by B3LYP/6-311++G(d,p) and B3PW91/LANL2DZ. Red color regions indicate the electron-withdrawing part and the blue color indicates the electron-donating part of the title molecules.

to the second and fourth benzene rings (from the left end) respectively indicates the electron-deficient nature of C═O bonds. This might be due to the involvement of electron-withdrawing oxygen atoms. Nitrogen atoms are less electronegative as compared to oxygen. Thus, the 4N—30H and 3N—29H bonds behave as the electron-rich moiety and impart electron donation. Therefore, the MEP

map of probe 2,9-DMQA indicates the possibility of intramolecular interactions between the C═O and N—H bonds. The N—H bonds as usual act as an electron-donating part after the introduction of Ag_3 and Au_3 clusters, but the electro-withdrawing region readily shifts towards the Ag_3 and Au_3 clusters. For 2,9DMQA + Ag_3, the electron-withdrawing surface that was observed over 16C═2O for probe molecule seems to be vanished and a light-yellow region was found to surround the Ag_3 trimer. Further shifting of the electron-withdrawing surface was observed for 2,9-DMQA + Au_3. The electron-withdrawing red regions in 2,9-DMQA + Au_3 were completely vanished from both the C═O bonds and more intense yellow surface was found over the Au_3 trimer. This can be interpreted as the Au_3 acts as strong electron-withdrawing as compared to the Ag_3. The intensity in color of the electron-withdrawing surface was further supported by the electrostatic potential where higher range of potential (shown in the color bar in Fig. 2 above the MEP surfaces) was observed for 2,9-DMQA + Au_3 ($\pm$ 7.09 $\times$ 10^{-2} V) as compared to 2,9-DMQA + Ag_3 ($\pm$ 8.19 $\times$ 10^{-2} V). Thus, the MEP surface establishes the involvement of the clusters in the intramolecular interactions and is in great agreement with the results from structural analysis. Therefore, the MEP surface analysis reveals the active participation of the Ag_3 and Au_3 clusters as electronegative moieties and shows the reactivity of the probe and the complexes.

3.3. Natural bond orbital and charge analysis

The property of charge transfer was discovered by the comparison between the natural charges obtained by NBOs and Mulliken charges. NBO analysis was performed for 2,9-DMQA, 2,9-DMQA + Ag_3, and 2,9-DMQA + Au_3 to get a better understanding of the charge delocalization from donor NBO to acceptor NBO, the higher will be the degree of conjugation which ensures complex stability. The Mulliken charges were obtained by the optimized geometries. The natural charge and the Mulliken charge distribution of all the atoms have been listed in SD 4 and Fig. 3 visualizes the comparison between both types of charges of 2,9-DMQA + Ag_3, and 2,9-DMQA + Au_3. Hydrogen atoms bonded to the carbon were all positive charge contributors while the carbon atoms of the benzene rings were positive as well as negative charge contributors. However, a change in the charges of the C═O and N—H bonds was observed. 1O and 2O have equal charges of − 0.338 e. The charge dissociation established by Mulliken and natural charge distribution was harmonious to the ICT shown by second-order perturbation theory analysis of the Fock Matrix in NBO calculations. *E(2)* was calculated for the 2,9-DMQA + Ag_3, and 2,9-DMQA + Au_3 for identifying the charge donor and acceptor moieties. In 2,9-DMQA + Ag_3 complex, the interaction between 2O and 43Ag had highest value of *E(2)* and in 2,9-DMQA + Au_3 complex, the interaction between 2O and 43Au had highest value of *E(2)*. Thus, the NBO analysis reveals the donor nature of 2O atom of 2,9-DMQA molecule. The donated charge cloud was accepted by the cluster in the respective complex. The 43Ag and 43Au were identified as the acceptor moieties in the 2,9-DMQA + Ag_3, and 2,9-DMQA + Au_3. Thus, the ICT was observed between the 2O atom of 2,9-DMQA and 43Ag and 43Au atom in clusters. To support the intramolecular interactions predicted by the Mulliken and natural charges, the Hirshfeld's surfaces has been discussed from our previously done study on photovoltaic study of 2,9-DMQA [60]. The Hirshfeld surface shown in reference paper shows the red regions nearby the C═O and N—H bonds. The red surface represents the moieties with high availability and deficiency of the charges. Ultimately, these surfaces are responsible for charge interactions. Moreover, the fingerprint plots in reference study gave prominent peaks for the N…H/H…N and C…O/O…C interactions. Thus, the Hirshfeld's surfaces gave promising results in the identification of the C═O and N—H as the bonds leading to the intramolecular interactions (Tables 2 and 3).

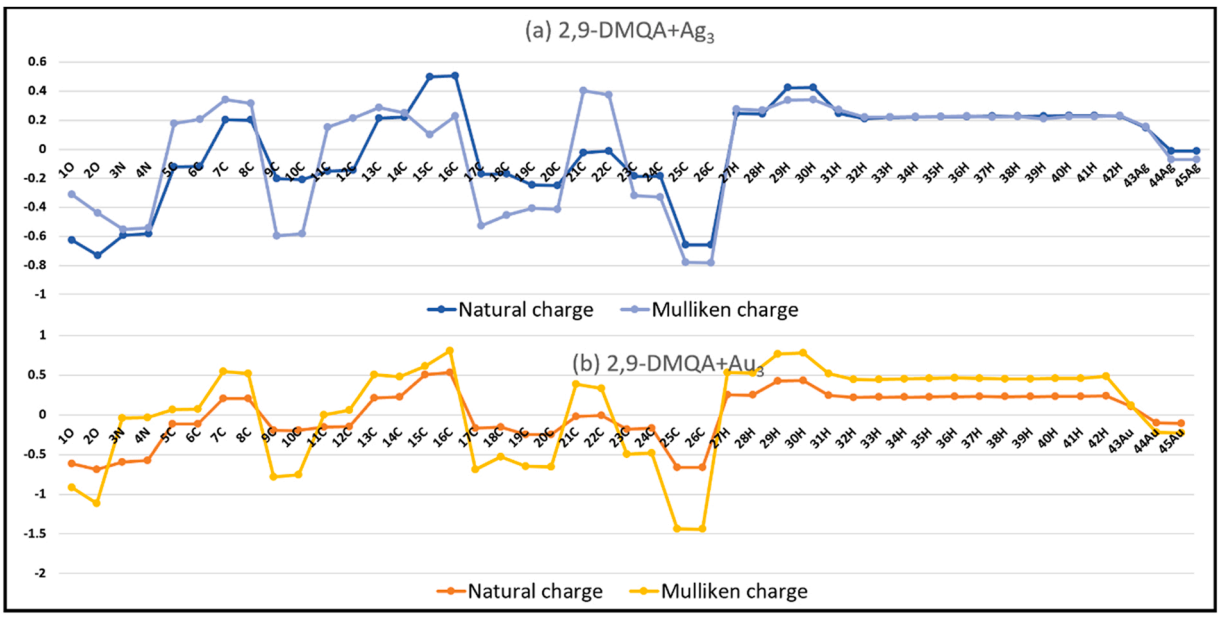

Fig. 3. Natural charge and Mulliken charge distribution of (a) 2,9-DMQA + Ag_3, and (b) 2,9-DMQA + Au_3.

Table 2
Second order perturbation theory analysis of Fock matrix in NBO Basis of 2,9-DMQA + Ag_3, 2,9-DMQA + Au_3 (LP-lone pair, LP*-anti-bond lone pair, BD-bonding orbital, BD*-antibonding orbital, CR-one center core pair).

S. no.	Donor NBO *(i)*	Acceptor NBO *(j)*	*E (2)* (kcal/mol)	*E (j)-E (i)* (au)	*F (i,j)* (au)
2,9-DMQA + Ag_3					
1.	LP (2) 2O	LP* (6) 43Ag	11.91	0.64	0.111
2.	LP (2) 2O	BD* (1) 43Ag – 44Ag	1.10	0.62	0.034
3.	LP (2) 2O	BD* (1) 43Ag – 45Ag	1.10	0.62	0.034
4.	LP (1) 2O	LP* (6) 43Ag	6.44	0.67	0.083
5.	CR (1) 2O	LP* (6) 43Ag	1.34	19.08	0.206
2,9-DMQA + Au_3					
1.	CR (1) 2O	LP* (6) 43Au	1.58	19.12	0.225
2.	LP (2) 2O	LP* (6) 43Au	15.93	0.68	0.134
3.	LP (2) 2O	BD* (1) 43–44Au	3.95	0.56	0.06
4.	LP (2) 2O	BD* (1) 43–45Au	3.91	0.56	0.06
5.	LP (4) 43Au	BD* (1) 18C – 32H	1.43	0.79	0.043
6.	LP (5) 43Au	BD* (2) 2O – 16C	1.07	0.25	0.023

Table 3
Frontier molecular orbital parameters for the 2,9-DMQA, 2,9-DMQA + Ag_3, and 2,9-DMQA + Au_3 (all values in eV and value of S is in eV^{-1}).

S no.	Molecular property	2,9-DMQA	2,9-DMQA + Ag_3	2,9-DMQA + Au_3
1.	E_{HOMO}	-5.52	-3.56	-5.95
2.	E_{LUMO}	-2.51	-2.72	-3.3
3.	Energy gap (ΔE)	3.01	2.87	2.65
4.	Ionization potential (*IP*)	5.52	3.56	5.95
5.	Electron affinity (*EA*)	2.51	2.72	3.3
6.	Chemical potential (*CP*)	-4.01	-3.14	-4.62
7.	Electronegativity (χ)	4.01	3.14	4.62
8.	Hardness (η)	1.5	1.43	1.32
9.	Softness (*S*)	0.66	0.69	0.75
10.	Electrophilicity index (ω)	5.36	3.44	8.08
11.	Electron accepting power (ω^{+})	3.53	10.21	5.92
12.	Electron donating power (ω^{-})	7.55	13.36	10.55

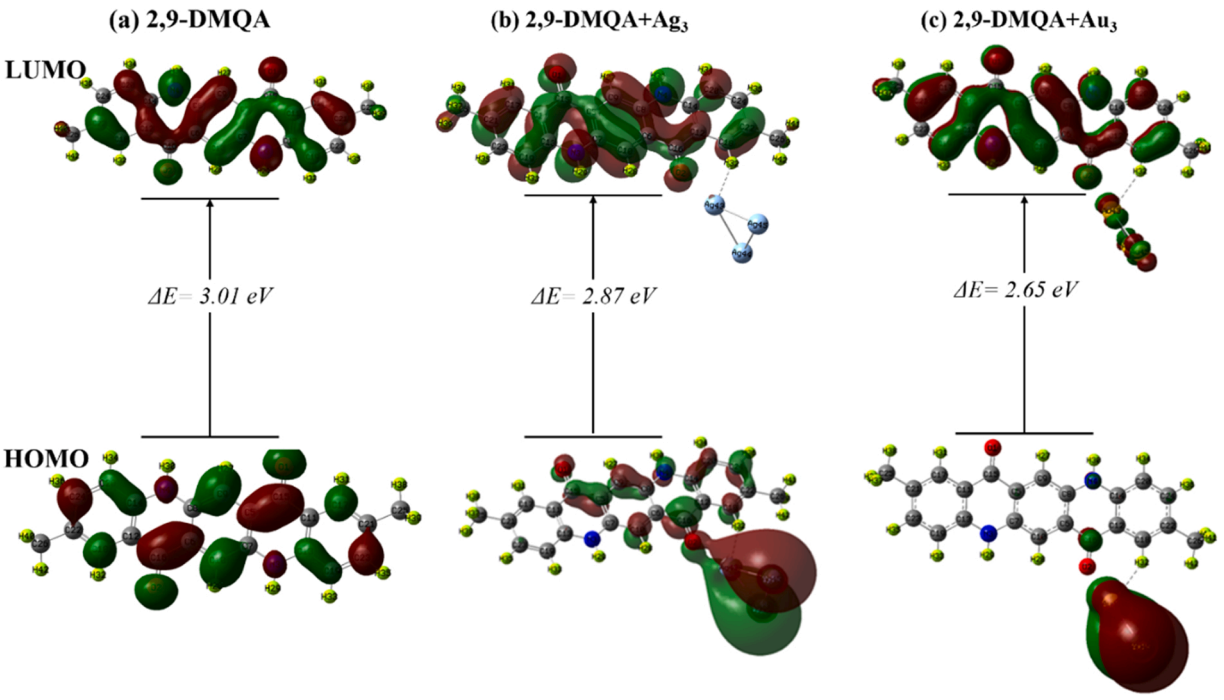

Fig. 4. HOMO-LUMO surfaces of (a) 2,9-DMQA, (b) 2,9-DMQA + Ag_3, and (c) 2,9-DMQA + Au_3.

3.4. Molecular orbital analysis

Energies corresponding to FMO were used to compute the global reactivity parameters. For probe 2,9-DMQA, the ΔE was computed as 3.01 eV. The introduction of Ag_3 and Au_3 clusters lead to the decrement in the ΔE of 2,9-DMQA + Ag_3 (2.87 eV) and 2,9-DMQA + Au_3 (2.65 eV). This could be due to the ability of Ag and Au to participate in the intramolecular interactions in 2,9-DMQA + Ag_3 and 2,9-DMQA + Au_3. The low value of ΔE indicates the easy transition of electrons from lower energy levels to higher energy levels [61]. The *IP* and *EA* values are analogous to the electron-donating and electron-accepting capabilities of the molecules. *IP* is analogous to the electron-donating activity of the molecule and low value of *IP* indicates that the molecule can easily donate the charge cloud for the interactions. Whereas the *EA* is the amount of energy of the molecule to accept the free charge cloud. 2, 9-DMQA + Ag_3 has the lowest value of *IP* (3.56 eV) which indicates the easy drifting of electrons in 2,9-DMQA due to the presence of Ag. The *EA* is highest for 2,9-DMQA + Au_3 showing its active participation in ICT reactions. The *CP* is the property of the molecules to lead the intramolecular interactions within the reactive moieties. 2,9-DMQA + Ag_3 has the highest value of *CP* (− 3.14 eV) showing that it has better capabilities to impart ICT other than probe 2,9-DMQA and 2,9-DMQA + Au_3. χ is defined as the chemical property of the withdrawing moiety of the molecule to attract the free charge cloud. The more the χ, the more the molecule will be able to donate the free electrons. Thus, 2,9-DMQA + Au_3 has the highest value of χ. The ω defines the lowering of energy due to maximal electron flow between *IP* and *EA*. η and S are the chemical parameters to describe the chemical hardness and softness of the of the materials. High values of chemical hardness and low value of softness reveal the rigidness and stiffness of the title compounds to get into the chemical reactions. Categorization of molecules is done as strong, moderate, and weak electrophiles for $\omega > 1.5$ eV, $0.8 < \omega < 1.5$ eV, and $\omega < 0.8$ eV [62]. The introduction of Ag_3 and Au_3 gives rise to the ω of the 2,9-DMQA, 2,9-DMQA + Ag_3, and 2,9-DMQA + Au_3. This validates the favorable energy transition between HOMO to LUMO. The higher values of ω^- for 2,9-DMQA, 2,9-DMQA + Ag_3, and 2, 9-DMQA + Au_3 indicates electron donating nature. The FMO analysis reveals that the chemical reactivity of the 2,9-DMQA experience a rise after the adsorption of Ag_3 and Au_3 clusters. Fig. 4 illustrates the HOMO-LUMO surfaces over the molecule and the complex. HOMO-LUMO surfaces locate the donor and acceptor orbitals in the molecular orbital wave function, respectively. The HOMO-LUMO surfaces show the participation of the C═O and N—H bonds in the 2,9-DMQA. However, the clusters adsorbed complex shows the involvement of clusters also. In 2,9-DMQA + Ag_3, the surfaces seem to dissociate from the cluster along with some nearby regions of the 2,9-DMQA to the overall geometry of 2,9-DMQA. Whereas, in 2,9-DMQA + Au_3, interactions were seen from the Au_3 cluster only to the 2,9-DMQA molecule. this shows the enhanced intramolecular interactions in 2,9-DMQA + Au_3 as compared to 2,9-DMQA + Ag_3. Therefore, the molecular orbital analysis reveals the existence of intramolecular interactions within the 2,9-DMQA + Ag_3, and 2, 9-DMQA + Au_3 complex.

3.5. Absorption and emission analysis

The electronic transitions were computed and studied for the title compound in the probe state and in the complex state using the TD-DFT calculations. The absorbance spectra and the emission spectra had been illustrated in Figs. 5 and 6. The other UV-Vis details had been listed in SD 5, 6, and 7. The absorption band of 2,9-DMQA comprises of two peaks one major and one minor. The major band falls in the range of 250–450 nm. The major band of 2,9-DMQA + Ag_3, and 2,9-DMQA + Au_3 shift to higher wavelengths between 350 and 700 nm. The absorption peak for 2,9-DMQA, 2,9-DMQA + Ag_3, and 2,9-DMQA + Au_3 were identified at 281 nm, 481 nm, and 504 nm with orbital transitions from HOMO-7 → LUMO, HOMO → LUMO + 5, and HOMO-1 → LUMO respectively. The absorption spectra were in great agreement with the HOMO-LUMO maps illustrated in Fig. 4. The HOMO in 2,9-DMQA + Ag_3 partially spread

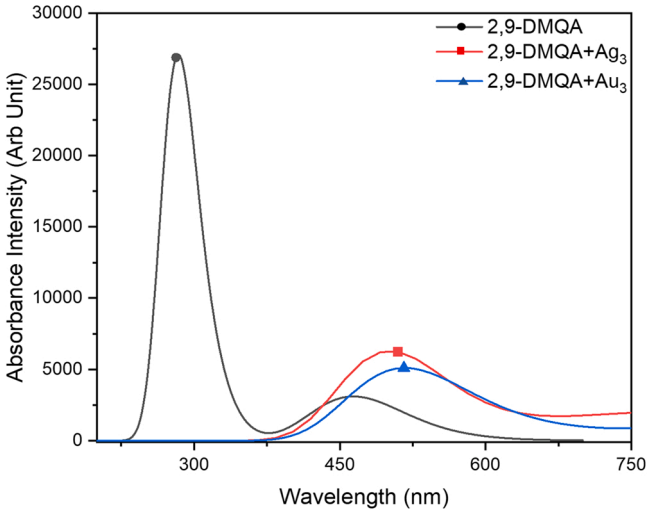

Fig. 5. Absorption spectra of 2,9-DMQA, 2,9-DMQA + Ag_3, and 2,9-DMQA + Au_3.

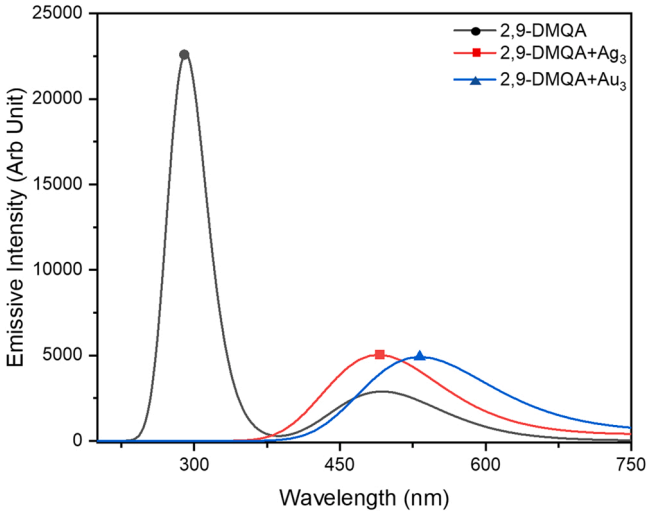

Fig. 6. Emission spectra of 2,9-DMQA, 2,9-DMQA + Ag_3, and 2,9-DMQA + Au_3.

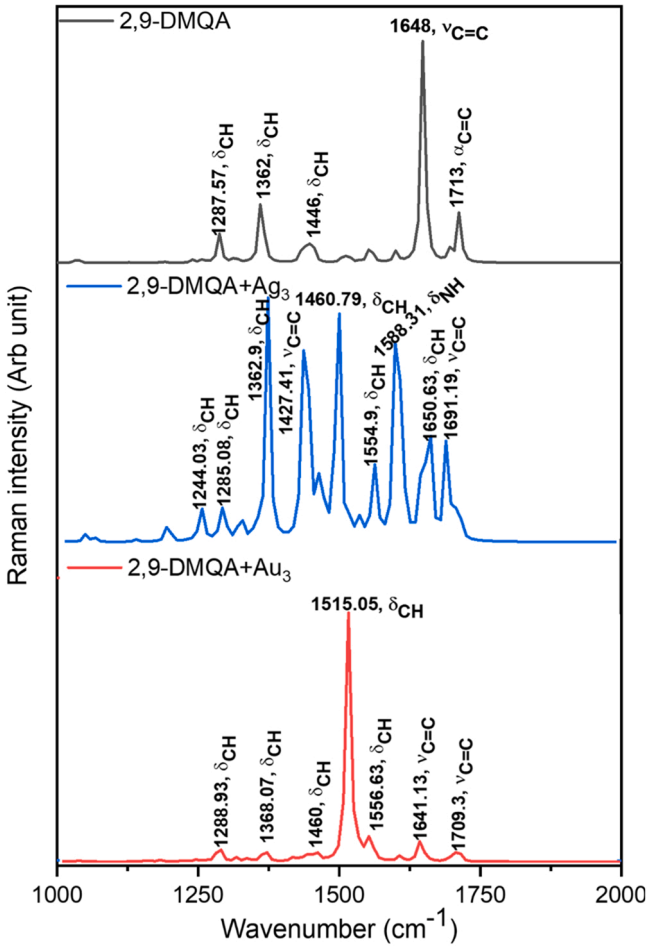

Fig. 7. Computed vibrational spectra of 2,9-DMQA, 2,9-DMQA + Ag_3, 2,9-DMQA + Au_3 molecule B3PW91/LANL2DZ basis set (Symmetric stretching-ν, torsional bending in plane (scissoring)-δ, Symmetric stretching-α).

over the Ag_3 (some part is localized over the molecule) and shifts from Ag_3 over the molecule. On the other hand, in the case of 2,9-DMQA + Au_3, the HOMO-LUMO surface is completely seen to shift from Au_3 over molecule indicating the involvement of Au_3 in the charge delocalization. There seems a shift in the wavelength of the absorbance band of 2,9-DMQA + Ag_3, and 2,9-DMQA + Au_3 which shows the active participation of clusters in enhancement of the intramolecular interactions. The absorption spectra of both the complex falls in the acceptable range for inducing the $\pi \rightarrow \pi^*$ transitions. Comparatively, 2,9-DMQA + Au_3 had higher wavelength. These results further correlate well with the structural parameters and the MEP plot.

The emission spectra computed for 2,9-DMQA was observed between 250 and 450 nm with its major peak at 289 nm and peak of minor band was at 493 nm. Emissive transition HOMO → LUMO leads to the formation of peak in the emissive spectra of 2,9-DMQA. Similar to absorption, a shift in the emission spectra of title molecule was observed after the introduction of Ag_3 and Au_3 clusters. The spectra of 2,9-DMQA + Ag_3 was obtained between 350 and 750 nm with its peak at 492 nm and emission spectra of 2,9-DMQA + Au_3 lies between 400 and 800 nm with peak 525 nm. This shows the higher emissive activity of 2,9-DMQA + Ag_3. Moreover, the range of emissive spectra of both the complex falls in the acceptable range of luminescence. However, the peak of emission spectra of 2,9-DMQA + Au_3 existed at higher wavelength than that of 2,9-DMQA + Ag_3. The UV-Vis analysis of the cluster adsorbed 2,9-DMQA indicates the high chemical reactivity of 2,9-DMQA + Au_3.

3.6. Vibrational analysis

The adsorption of Ag_3 and Au_3 on 2,9-DMQA was further studied using vibrational modes. The computed vibrational spectra for 2,9-DMQA, 2,9-DMQA + Ag_3, and 2,9-DMQA + Au_3 are shown in Fig. 7 and the major vibrations with high Raman intensity had been listed in SD 8. The major vibrational peaks of 2,9-DMQA were observed between 1250 and 1750 cm^{-1}. The torsional bending (δ_{CH}) modes majorly occur between frequencies 1200–1500 cm^{-1}. C═C linear stretching (ν_{CC}) occurring at 1648 cm^{-1} was observed to have the highest Raman intensity. It was observed that the adsorption of Ag_3 and Au_3 causes a significant enhancement in the Raman intensity of some of the vibrational species. For 2,9-DMQA + Ag_3, multiple Raman peaks were observed in between 1200 and 1700 cm^{-1}. These peaks include δ_{CH}, δ_{NH}, and ν_{CC}. δ_{CH} for 2,9-DMQA + Ag_3 has high peaks around 1244.03, 1362.9, and 1460.79 cm^{-1}. ν_{CC} for 2,9-DMQA + Ag_3 has a high-intensity peak at 1427.41 cm^{-1}. All the vibrational modes of Ag – Ag, and Au – Au were at low frequencies. The δ_{CH} observed at 1362.9 cm^{-1} was observed for 18C—32H bond that is the connecting bond between the 2,9-DMQA and Ag_3. This mode δ_{CH} between 18C and 32H for 2,9-DMQA + Ag_3 has the highest Raman intensity at frequency 1679.8 cm^{-1} among the other vibrational modes. Similarly, for 2,9-DMQA + Au_3, the δ_{CH} between 18C and 32H had the highest Raman intensity at frequency 1515.05 cm^{-1}. The highest Raman intensity indicates 18C – 32H as the perfect adsorption site for Ag_3 and Au_3 clusters. Moreover, the Raman intensity for the $\delta_{18C-32H}$ of 2,9-DMQA + Au_3 was higher than that of δ_{CH} in 2,9-DMQA + Ag_3. This supports the better adsorption in case of 2,9-DMQA + Au_3 as compared to 2,9-DMQA + Ag_3. High Raman intensity obtained for δ_{CH} of 18C – 32H better supports the interaction shown in the MEP surfaces of 2,9-DMQA + Ag_3, 2,9-DMQA + Au_3. In Fig. 2, the dotted line between the clusters and 2,9-DMQA nearby 18C – 32H shows interactions between the cluster and probe molecule. thus, it can be stated that the region with the highest Raman intensity for the vibrations is the target place of the adsorption for the clusters. This confirms the interactions taking place between the molecule and the metal surfaces involved. Moreover, the high Raman modes were obtained for 2,9-DMQA + Au_3. The higher Raman intensity leads to a high value of hyperpolarizability of the molecule. Thus, the vibrational analysis also concludes the high hyperpolarizability and thus high NLO activity of 2,9-DMQA + Au_3.

3.7. Linear and nonlinear optical activity

NLO activity of the molecule and the complexes was established using the polarizability and hyperpolarizability parameters. As the NLO materials have high ICT, they must have high hyperpolarizability [63]. So, the polarizability and hyperpolarizability parameters were computed for 2,9-DMQA, 2,9-DMQA + Ag_3, and 2,9-DMQA + Au_3 to check whether the adsorption of Ag_3 and Au_3 clusters leads to any increment in the NLO activity. The same parameters were also computed for a dimer (Ag_2 and Au_2) and tetramer (Ag_4 and Au_4) adsorbed 2,9-DMQA to justify the selection of trimers adsorbed 2,9-DMQA as potent NLO active complexes. α_{total} and $\Delta\alpha$ are the parameters that show the optical linearity of the molecule. However, β_{total} is the higher-order term that reflects the optical nonlinearity of the molecule. The computed values of the α_{total}, $\Delta\alpha$, and β_{total} for all complexes are listed in Table 4. The tensor components of polarizability parameters for the trimer complex are listed in SD 9 and 10. The value of the α_{total} for the 2,9-DMQA, 2,9-DMQA + Ag_3, and 2,9-DMQA + Au_3 are computed as 51.66×10^{-24}, 121.27×10^{-24}, and 77.13×10^{-24} esu respectively. $\Delta\alpha$ has values 136.55×10^{-24}, 429.42×10^{-24}, and 225.09×10^{-24} esu for 2,9-DMQA, 2,9-DMQA + Ag_3, and 2,9-DMQA + Au_3. The values of polarizability parameters for 2,9-DMQA + Ag_3, and 2,9-DMQA + Au_3 seem to rise after the adsorption of the clusters. However, the values of α_{total} and $\Delta\alpha$ for 2,9-DMQA + Ag_2, 2,9-DMQA + Au_4, 2,9-DMQA + Au_2, and 2,9-DMQA + Au_4 were not significantly higher than the probe 2,9-DMQA. The value of α_{total} and $\Delta\alpha$ for 2,9-DMQA + Ag_3 was observed high as compared to that of 2,9-DMQA + Au_3. This indicates the linear opticality of the 2,9-DMQA + Ag_3 complex. The value of β_{total} for a probe was computed as 0.001416×10^{-30} esu which is very low. This indicates that the 2,9-DMQA molecule doesn't have any NLO activity in the probe state. But, when the Ag_3 and Au_3 clusters were introduced to the probe, a massive rise in the value of the β_{total} was observed. The value of the β_{total} for 2,9-DMQA + Ag_3 and 2,9-DMQA + Au_3 were computed as 1066.85×10^{-30} esu and 1163.07×10^{-30} esu. These values are extremely higher than the β_{total} of the most generally used reference material Urea (0.78×10^{-30} esu) [64]. Moreover, the computed values of β_{total} for 2,9-DMQA + Ag_2, 2,9-DMQA + Au_4, 2,9-DMQA + Au_2, and 2,9-DMQA + Au_4 were also comparatively lower than the values of same for 2,9-DMQA + Ag_3 and 2,9-DMQA + Au_3. For better validation of the NLO activity of the designed complex, the β_{total} of the title complex was compared with already designed and proven complex by Felscia et al. by making Ag_3, and Au_3 clusters adsorbed on

Table 4
Computed values of μ_{total}, α_{total}, $\Delta\alpha$, and β_{total} for the complexes ($\boldsymbol{\mu_{total}}$ is in Debye and, α_{total}, $\Delta\alpha$, and β_{total} values are in esu).

Molecule	μ_{total}	α_{total}	$\Delta\alpha$	β_{total}
2,9-DMQA	0.00007	51.66×10^{-24}	136.55×10^{-24}	0.001416×10^{-30}
2,9-DMQA + Ag_2	3.75	58.2×10^{-24}	145.88×10^{-24}	5.561×10^{-30}
2,9-DMQA + Ag_3	6.95	121.27×10^{-24}	429.42×10^{-24}	1066.85×10^{-30}
2,9-DMQA + Ag_4	3.65	88.92×10^{-24}	235.11×10^{-24}	1001.64×10^{-30}
2,9-DMQA + Au_2	5.77	58.19×10^{-24}	145.97×10^{-24}	5.56×10^{-30}
2,9-DMQA + Au_3	6.95	77.13×10^{-24}	225.09×10^{-24}	1163.07×10^{-30}
2,9-DMQA + Au_4	6.49	74.04×10^{-24}	179.33×10^{-24}	115.96×10^{-30}

the QA. In the reference study, the value of the β_{total} was found to be 930.81×10^{-30} esu, and 120.8×10^{-30} esu for silver and gold trimers complexed with QA respectively. These values are relatively lower than the β_{total} of the 2,9-DMQA + Ag_3, and 2,9-DMQA + Au_3 [35]. This shows that the 2,9-DMQA complexes have higher NLO activity than the QA complexes. The comparison between 2,9-DMQA + Ag_3, and 2,9-DMQA + Au_3, reveals the high NLO activity of 2,9-DMQA + Au_3.

4. Conclusion

The NLO activity of Ag_3 and Au_3 adsorbed 2,9-DMQA was reported in the present study. The interaction energy and the dipole moment were found larger for the 2,9-DMQA + Au_3. The NBO calculations done for the complex shows that C═O and N–H moieties in 2,9-DMQA were involved in intramolecular interactions, but after the introduction of Ag_3 and Au_3, it was observed that these clusters were majorly involved in the intramolecular interactions. The MEP surface was in good agreement with the NBO calculations and identifies the N–H moieties as the donor and the C═O moieties as the acceptor moieties. However, the Ag_3 and Au_3, act as the acceptor in 2,9-DMQA + Ag_3 and 2,9-DMQA + Au_3 and impart in the intramolecular interactions. The charge transfer was identified from 2O to 43Ag in 2,9-DMQA + Ag_3 and 2O to 43Au in 2,9-DMQA + Au_3. The computed values of FMO parameters reveal the rise in reactivity of the 2,9-DMQA after the adsorption of clusters. The absorption and emission spectra for the 2,9-DMQA, 2,9-DMQA + Ag_3, and 2,9-DMQA + Au_3 highlights the possibility of ICT in the probe and complexes. The computed Raman vibration corresponding 18C – 32H was found to have highest value of Raman intensity as compared to the torsional bending of other bonds. The high Raman intensity indicates the adsorption site for the clusters over the bond 18C—32H. The linear optical parameters had higher values for 2,9-DMQA + Ag_3 and NLO parameters had higher values for 2,9-DMQA + Au_3. Hence, 2,9-DMQA + Au_3 had higher NLO activity. Thus, from the following study, it can be concluded that the 2,9-DMQA adsorbed with Ag_3, and Au_3 clusters possess better NLO activity and this study can better be a basis for experimental demonstrations. Therefore, the present study gives insights into the fruitful experimental proceeding of development of the NLO material from 2,9-DMQA + Au_3.

CRediT authorship contribution statement

Shradha Lakhera: Data curation, Writing – original draft, Visualization, Investigation, Software, Validation. **Meenakshi Rana:** Conceptualization, Methodology, Writing – review & editing, Supervision**. Kamal Devlal:** Conceptualization, Writing – review & editing**. Vivek Dhuliya:** Visualization, Investigation, Software, Validation. **Nupur Pandey:** Visualization, Software.

Declaration of Competing Interest

The authors declare that they have no known competing financial interests or personal relationships that could have appeared to influence the work reported in this paper.

Data Availability

Data used for the research is described in the article.

Appendix A. Supporting information

Supplementary data associated with this article can be found in the online version at doi:10.1016/j.ijleo.2023.170983.

References

[1] S. Lakhera, K. Devlal, M. Rana, V. Dhuliya, Quantum mechanical study of three aromatic bioactive fatty alcohol compounds with nonlinear optical and potential light harvesting properties, Opt. Mater. 129 (2022), 112476, https://doi.org/10.1016/j.optmat.2022.112476.
[2] M. Rana, N. Singla, A. Pathak, R. Dhanya, C. Narayana, P. Chowdhury, Vibrational-electronic properties of intra/inter molecular hydrogen bonded heterocyclic dimer: an experimental and theoretical study of pyrrole-2-carboxaldehyde, Vib. Spectrosc. 89 (2017) 16–25, https://doi.org/10.1016/j.vibspec.2016.12.003.

[3] M. Rana, N. Singla, A. Chatterjee, A. Shukla, P. Chowdhury, Investigation of nonlinear optical (NLO) properties by charge transfer contributions of amine functionalized tetraphenylethylene, Opt. Mater. 62 (2016) 80–89, https://doi.org/10.1016/j.optmat.2016.09.043.

[4] M. Rana, P. Chowdhury, Nonlinear optical responses of organic based indole derivative: an experimental and computational study, Mater. Today: Proc. 28 (1) (2020) 241–245, https://doi.org/10.1016/j.matpr.2020.01.598.

[5] S. Lakhera, K. Devlal, A. Ghosh, M. Rana, Modelling the DFT structural and reactivity study of feverfew and evaluation of its potential antiviral activity against COVID-19 using molecular docking and MD simulations, Chem. Pap. 76 (2022) 2759–2776, https://doi.org/10.1007/s11696-022-02067-6.

[6] S. Yamashita, A tutorial on nonlinear photonic applications of carbon nanotube and graphene, J. Light. Technol. 30 (4) (2012) 427–447, https://doi.org/10.1109/JLT.2011.2172574.

[7] S. Yu, X. Wang, Y. Ai, X. Tan, T. Hayat, W. Hu, X. Wang, Experimental and theoretical studies on competitive adsorption of aromatic compounds on reduced graphene oxides, J. Mater. Chem. A 4 (2016) 5654–5662, https://doi.org/10.1039/C6TA00890A.

[8] J. Maria, K. Iqbal, K. Ayub, Enhanced electronic and non-linear optical properties of alkali metal (Li, Na, K) doped boron nitride nano-cages, J. Alloy. Compd. 687 (2016) 976–983, https://doi.org/10.1016/j.jallcom.2016.06.121.

[9] S. Munsif, Maria, S. Khan, A. Ali, M.A. Gilani, J. Iqbal, R. Ludwig, K. Ayub, Remarkable nonlinear optical response of alkali metal doped aluminum phosphide and boron phosphide clusters, J. Mol. Liq. 271 (2018) 51–64, https://doi.org/10.1016/j.molliq.2018.08.121.

[10] H. Alyar, A review on nonlinear optical properties of donor-acceptor derivatives of naphthalene and azanapthelene, Rev. Adv. Mater. Sci. 34 (2013) 79–87.

[11] S. Lakhera, K. Devlal, M. Rana, I. Celik, Study of nonlinear optical responses of phytochemicals of Clitoria ternatea by quantum mechanical approach and investigation of their anti-Alzheimer activity with in silico approach, Struct. Chem. (2022), https://doi.org/10.1007/s11224-022-01981-5.

[12] P.S. Halasyamani, W. Zhang, Inorganic Materials for UV and Deep-UV Nonlinear Optical Applications, ACS Publications, 2017.

[13] D.T. Chase, A.G. Fix, B.D. Rose, C.D. Weber, S. Nobusue, C.E. Stockwell, L.N. Zakharov, M.C. Lonergan, M.M. Haley, Electron-accepting 6,12-diethynylindeno [1,2-b]fluorenes: synthesis, crystal structures, and photophysical properties, Angew. Chem. Int. Ed. 50 (47) (2011) 11103–11106, https://doi.org/10.1002/anie.201104797.

[14] B. Zhang, G. Shi, Z. Yang, F. Zhang, S. Pan, Fluorooxoborates: beryllium-free deepultraviolet nonlinear optical materials without layered growth, Angew. Chem. Int. Ed. 56 (14) (2017) 3916–3919, https://doi.org/10.1002/anie.201700540.

[15] R.D. Fonseca, M.G. Vivas, D.L. Silva, G. Eucat, Y. Bretonnière, C. Andraud, L. De Boni, C.R. Mendonça, First-order hyperpolarizability of triphenylamine derivatives containing cyanopyridine: molecular branching effect, J. Phys. Chem. C 122 (3) (2018) 1770–1778, https://doi.org/10.1021/acs.jpcc.7b05829.

[16] L. Guo, Z. Guo, X. Li, Design and preparation of side chain electro-optic polymeric materials based on novel organic second order nonlinear optical chromophores with double carboxyl groups, J. Mater. Sci.: Mater. Electron. 29 (3) (2018) 2577–2584, https://doi.org/10.1007/s10854-017-8181-y.

[17] F. Liu, Y. Yang, H. Wang, J. Liu, C. Hu, F. Huo, S. Bo, Z. Zhen, X. Liu, L. Qiu, Comparative studies on structure–nonlinearity relationships in a series of novel second-order nonlinear optical chromophores with different aromatic amine donors, Dyes Pigments 120 (2015) 347–356, https://doi.org/10.1039/C5TC02702K.

[18] H. Claus, C.D. Bradford, S. Alexandra, C. Alessia, D. Claudia, R. Stefania, R. Dominique, J. Denis, Z.C. Eli, G. Veronique, An investigation on the second-order nonlinear optical response of cationic bipyridine or phenanthroline iridium(III) complexes bearing cyclometallated 2-phenylpyridines with a triphenylamine substituent, Dalton Trans. (2018), https://doi.org/10.1039/C8DT00754C.

[19] C. Dragonetti, S. Righetto, D. Roberto, R. Ugo, A. Valore, S. Fantacci, A. Sgamellotti, F. De Angelis, Cyclometallated iridium (III) complexes with substituted 1, 10-phenanthrolines: a new class of highly active organometallic second order NLO-phores with excellent transparency with respect to second harmonic emission, Chem. Commun. 40 (2007) 4116–4118.

[20] A. Mahmood, M.I. Abdullah, M.F. Nazar, Quantum chemical designing of novel organic non-linear optical compounds, BKCS 35 (5) (2014) 1391–1396, https://doi.org/10.5012/bkcs.2014.35.5.1391.

[21] A. Mahmood, M.I. Abdullah, S.U. Khan, Enhancement of nonlinear optical (NLO) properties of indigo through modification of auxiliary donor, donor and acceptor, Spectrochim. Acta Part B Spectrosc. 139 (2015) 425–430, https://doi.org/10.1016/j.saa.2014.12.038.

[22] A. Mahmood, A. Irfan, J.L. Wang, Molecular level understanding of the chalcogen atom effect on chalcogen-based polymers through electrostatic potential, non-covalent interactions, excited state behaviour, and radial distribution function, Polym. Chem. 13 (2022) 5993–6001, https://doi.org/10.1039/D2PY00960A.

[23] S. Lakhera, K. Devlal, A. Ghosh, M. Rana, In silico investigation of phytoconstituents of medicinal herb 'Piper Longum' against SARS-CoV-2 by molecular docking and molecular dynamics analysis, Results Chem. 3 (2021), 100199, https://doi.org/10.1016/j.rechem.2021.100199.

[24] M. Rana, P. Chowdhury, Nonlinear optical responses of organic based indole derivative: an experimental and computational study, Mater. Today: Proc. 28 (1) (2020) 241–245, https://doi.org/10.1016/j.matpr.2020.01.598.

[25] M.U. Khan, M. Khalid, R.A. Khera, M.N. Akhtar, A. Abbas, M.F. Rehman, A.A.C. Braga, M.M. Alam, M. Imran, Y. Wang, C. Lu, Influence of acceptor tethering on the performance of nonlinear optical properties for pyrene-based materials with A-π-D-π-D architecture, Arab. J. Chem. 15 (3) (2022), 103673, https://doi.org/10.1016/j.arabjc.2021.103673.

[26] S. Lakhera, M. Rana, K. Devlal, V. Dhuliya, Computational study of non-linear optical and electrical properties of 1,3-dinitropyrene, Opt. Quant. Electron. 55 (2023) 85, https://doi.org/10.1007/s11082-022-04371-7.

[27] A. Gowda, L. Jacob, A. Patra, A. George, R. Philip, S. Kumar, Synthesis, mesomorphic properties and nonlinear optical studies of alkyl and alkoxy phenylacetylene containing phenazine fused extended triphenylene discotic liquid crystalline dyes, Dyes Pigments 160 (2019) 128–135, https://doi.org/10.1016/j.dyepig.2018.07.052.

[28] W. Liszewski, E.M. Warshaw, Pigments in American tattoo inks and their propensity to elicit allergic contact dermatitis, JAAD 81 (2) (2019) 379–385, https://doi.org/10.1016/j.jaad.2019.01.078.

[29] I.K. Bajer, M. Guzauskas, M.M. Janusik, M. Zagórska, M. Mahmoudi, J.V. Grazulevicius, A. Proń, D. Volyniuk, Acridone and quinacridone derivatives with carbazole or phenoxazine substituents: synthesis, electrochemistry, photophysics and application as TADF electroluminophores, J. Mater. Chem. C 10 (2022) 12377–12391, https://doi.org/10.1039/D2TC02270B.

[30] P. Devibala, B. Balambiga, S. Noureen, S. Nagarajan, Hexaarylbenzene based high-performance p-channel molecules for electronic applications, RSC Adv. 11 (2021) 11672–11701, https://doi.org/10.1039/d1ra00217a.

[31] P. Gómez, S. Georgakopoulos, M.M. Montoya, J. Cerdá, J. Pérez, E. Ortí, J. Aragó, D. Curiel, Improving the robustness of organic semiconductors through hydrogen bonding, ACS Appl. Mater. Interfaces 13 (7) (2021) 8620–8630, https://doi.org/10.1021/acsami.0c18928.

[32] J. Jia, C. Hu, Y. Cui, Y. Li, W. Wang, L. Han, Y. Li, J. Gao, Design and synthesis of a series of N-donor quinacridone derivatives with novel nonlinear optical properties, Dyes Pigments 149 (2018) 843–850, https://doi.org/10.1016/j.dyepig.2017.11.056.

[33] J. Jia, Y. Li, W. Wang, C. Luo, L. Han, Y. Li, J. Gao, New quinacridone derivatives: structure-function relationship exploration to enhance third-order nonlinear optical responses, Dyes Pigments 146 (2017) 251–262, https://doi.org/10.1016/j.dyepig.2017.06.026.

[34] J. Jia, D. Feng, Y. Sha, C. Zhou, G. Liang, Y. She, New quinacridone derivatives: synthesis, photophysical and third-order nonlinear optical properties, Tetrahedron 76 (16) (2020), 131057, https://doi.org/10.1016/j.tet.2020.131057.

[35] U.R. Felscia, B.J.M. Rajkumar, Computational study of quinacridone on silver and gold clusters: applications to organic light emitting diodes and nonlinear optical devices, Mater. Lett. (2018), https://doi.org/10.1016/j.matlet.2018.03.149.

[36] R. Deska, J.O. Banska, E.D. Głowacki, M. Samoc, K. Matczyszyn, Two-photon excited luminescence and second-harmonic generation in quinacridone microstructures, Dyes Pigments 177 (2020), 108268, https://doi.org/10.1016/j.dyepig.2020.108268.

[37] Y. Cui, G. Liang, J. Jia, G. Yu, Y. Sha, C. Zhou, Y. She, Study on new quinacridone derivatives with enhanced third-order nonlinear optical properties, Tetrahedron 76 (22) (2020), 131169, https://doi.org/10.1016/j.tet.2020.131169.

[38] Z. Liu, Xiao Yang, Zongfan Yang, Xi Su, Zhen Xie, Weihua Chen, Wenqin Zhang, Long Chen, Quinacridone based 2D covalent organic frameworks as efficient photocatalysts for aerobic oxidative Povarov reaction, Appl. Catal. 312 (2022), 121406, https://doi.org/10.1016/j.apcatb.2022.121406.

[39] S.E. Shaheen, B. Kippelen, N. Peyghambarian, Energy and charge transfer in organic light-emitting diodes: a soluble quinacridone study, J. Appl. Phys. 85 (1999) 7939, https://doi.org/10.1063/1.370612.

[40] I. Chaban, R. Deska, G. Privault, E. Trzop, M. Lorenc, S.E. Kooi, K.A. Nelson, M. Samoc, K. Matczyszyn, T. Pezeril, Nonlinear optical absorption in nanoscale films revealed through ultrafast acoustics, Nano Lett. 22 (11) (2022) 4362–4367, https://doi.org/10.1021/acs.nanolett.2c00771.
[41] S. Jeyaram, J. Naseer, S. Punitha, Effect of solvent on third-order nonlinear optical behavior of reactive blue 19 dye, J. Fluor. 31 (2021) 1895–1906, https://doi.org/10.1007/s10895-021-02808-y.
[42] U.R. Felscia, B.J.M. Rajkumar, P. Sankar, R. Philip, M.B. Mary, Theoretical and experimental investigations of nitropyrene on silver for nonlinear optical and metal ion sensing applications, Mater. Chem. Phys. (2019), https://doi.org/10.1016/j.matchemphys.2019.122466.
[43] A. Irudaya Jothi, M. Wilson Bosco Paul, V. Alexander, A comparative molecular structure – NLO activity study of ortho-bridged dibenzaldehydes: synthesis, crystal structure, SHG, and DFT studies, J. Mol. Struct. 1250 (2) (2022), 131776, https://doi.org/10.1016/j.molstruc.2021.131776.
[44] R. Zaier, S. Ayachi, DFT molecular modeling studies of D-π-A-π-D type cyclopentadithiophene-diketopyrrolopyrrole based small molecules donor materials for organic photovoltaic cells, Optik 239 (2021), 166787, https://doi.org/10.1016/j.ijleo.2021.166787.
[45] F.A. Sahki, A. Bouraiou, S. Taboukhat, L. Messaadia, S. Bouacida, V. Figa, K. Bouchouit, B. Sahraoui, Design and synthesis of highly conjugated electronic phenanthrolines derivatives for remarkable NLO properties and DFT analysis, Optik 241 (2021), 166949, https://doi.org/10.1016/j.ijleo.2021.166949.
[46] M. Vennila, R. Rathikha, S. Muthu, A. Jeelani, Ahmad Irfan, Theoretical structural analysis (FT-IR, FT-R), solvent effect on electronic parameters NLO, FMO, NBO, MEP, UV (IEFPCM model), Fukui function evaluation with pharmacological analysis on methyl nicotinate, Comput. Theor. Chem. 1217 (2022), 113890, https://doi.org/10.1016/j.comptc.2022.113890.
[47] A. Saral, P. Sudha, S. Muthu, S. Sevvanthi, Ahmad Irfan, Molecular structure spectroscopic Elucidation, IEFPCM solvation (UV–Vis, MEP, FMO, NBO, NLO), molecular docking and biological assessment studies of lepidine (4-Methylquinoline), J. Mol. Liq. 345 (2022), 118249, https://doi.org/10.1016/j.molliq.2021.118249.
[48] A. Irfan, A.G.A. Sehemi, M.A. Assiri, S. Ullah, Exploration the effect of metal and electron withdrawing groups on charge transport and optoelectronic nature of schiff base Ni(II), Cu(II) and Zn(II) complexes at molecular and solid-state bulk scales, Mater. Sci. Semicond. Process. 107 (2020), 104855, https://doi.org/10.1016/j.mssp.2019.104855.
[49] D.V. Velayudhan, S.H. Cherumuttathu, Design and DFT study of nitrogen-rich donor systems for improved photovoltaic performance in dye-sensitized solar cells, New J. Chem. 45 (2021) 11585–11595, https://doi.org/10.1039/D1NJ00881A.
[50] K. Arulaabaranam, S. Muthu, G. Mani, Ahmad Irfan, Conformational study, FT-IR, FT-Raman, solvent effect on UV–Vis, charge transfer and protein–ligand interactions of methyl-2-pyrazinecarboxylate, J. Mol. Liq. 341 (2021), 116934, https://doi.org/10.1016/j.molliq.2021.116934.
[51] M.J. Frisch, Gaussian 09, Revision B.01, Gaussian Inc., Wallingford CT, 2010.
[52] C.J. Cramer, D.G. Truhlar, Density functional theory for transition metals and transition metal chemistry, Phys. Chem. Chem. Phys. 11 (2009) 10757–10816, https://doi.org/10.1039/B907148B.
[53] S.F. Boys, F. Bernardi, The calculation of small molecular interactions by the differences of separate total energies: some procedures with reduced errors, Mol. Phys. 19 (1970) 553–556.
[54] S. Grimme, J. Antony, S. Ehrlich, H. Krieg, A consistent and accurate ab initio parameterization of density functional dispersion correction (DFT-D) for the 94 elements H-Pu, J. Chem. Phys. 132 (2010), 154104, https://doi.org/10.1063/1.3382344.
[55] M. Rana, N. Singla, A. Pathak, D.R.C. Narayana, P. Chowdhury, Vibrational-electronic properties of intra/inter molecular hydrogen bonded heterocyclic dimer: an experimental and theoretical study of pyrrole-2-carboxaldehyde, Vibr. Spectrosc. ⟨https://doi.org/10.1016/j.vibspec.2016.12.003⟩.
[56] T. Koopmans, Ordering of wave functions and eigenenergies to the individual electrons of an atom, Physica 1 (1933) 104–113, https://doi.org/10.1016/S0031-8914(34)90011-2.
[57] O. Gritsenko, E.J. Baerends, The analog of Koopmans' theorem for virtual Kohn–Sham orbital energies, Can. J. Chem. 87 (2009), https://doi.org/10.1139/V09-088.
[58] S. Lakhera, M. Rana, K. Devlal, Influence of adsorption of gold and silver nanoclusters on structural, electronic, and nonlinear optical properties of pentacene-5, 12-dione: a DFT study, Opt. Quant. Electron. 55 (2023) 178, https://doi.org/10.1007/s11082-022-04422-z.
[59] P. Yadav, M. Rana, P. Chowdhury, DFT and MD simulation investigation of favipiravir as an emerging antiviral option against viral protease (3CLpro) of SARS-CoV-2, J. Mol. Struct. 1246 (2021), 131253, https://doi.org/10.1016/j.molstruc.2021.131253.
[60] S. Lakhera, M. Rana, K. Devlal, N. Kanagathara, J. Janczak, Photovoltaic characteristics of organic heterocyclic2,9-dimethyl quinacridone in different solvents using DFT approach, J. Photochem. Photobiol. A: Chem. (2023), 114664, https://doi.org/10.1016/j.jphotochem.2023.114664.
[61] S. Lakhera, M. Rana, K. Devlal, I. Celik, R. Yadav, A comprehensive exploration of pharmacological properties, bioactivities and inhibitory potentiality of luteolin from Tridax procumbens as anticancer drug by in-silico approach, Struct. Chem. (2022), https://doi.org/10.1007/s11224-022-01882-7.
[62] L.R. Domingo, P. Pérez, The nucleophilicity N index in organic chemistry, Org. Biomol. Chem. 9 (2011) 7168–7175, https://doi.org/10.1039/C1OB05856H.
[63] S. Lakhera, M. Rana, K. Devlal, Theoretical study on spectral and optical properties of essential amino acids: a comparative study, Opt. Quantum Electron. 54 (2022) 714, https://doi.org/10.1007/s11082-022-04118-4.
[64] C. Cassidy, J.M. Halbout, W. Donaldson, C.L. Tang, Nonlinear optical properties of urea, Opt. Commun. 29 (2) (1979) 243–246, https://doi.org/10.1016/0030-4018(79)90027-0.